

# Methods for Estimating Dose from Galactic Cosmic Rays and Jovian Radiation Belts on Reduced-Order Monte Carlo Geometries



Mathew W. Swinney  
Michael B. R. Smith

**August 2021**

### DOCUMENT AVAILABILITY

Reports produced after January 1, 1996, are generally available free via US Department of Energy (DOE) SciTech Connect.

**Website** [www.osti.gov](http://www.osti.gov)

Reports produced before January 1, 1996, may be purchased by members of the public from the following source:

National Technical Information Service  
5285 Port Royal Road  
Springfield, VA 22161  
**Telephone** 703-605-6000 (1-800-553-6847)  
**TDD** 703-487-4639  
**Fax** 703-605-6900  
**E-mail** [info@ntis.gov](mailto:info@ntis.gov)  
**Website** <http://classic.ntis.gov/>

Reports are available to DOE employees, DOE contractors, Energy Technology Data Exchange representatives, and International Nuclear Information System representatives from the following source:

Office of Scientific and Technical Information  
PO Box 62  
Oak Ridge, TN 37831  
**Telephone** 865-576-8401  
**Fax** 865-576-5728  
**E-mail** [reports@osti.gov](mailto:reports@osti.gov)  
**Website** <https://www.osti.gov/>

This report was prepared as an account of work sponsored by an agency of the United States Government. Neither the United States Government nor any agency thereof, nor any of their employees, makes any warranty, express or implied, or assumes any legal liability or responsibility for the accuracy, completeness, or usefulness of any information, apparatus, product, or process disclosed, or represents that its use would not infringe privately owned rights. Reference herein to any specific commercial product, process, or service by trade name, trademark, manufacturer, or otherwise, does not necessarily constitute or imply its endorsement, recommendation, or favoring by the United States Government or any agency thereof. The views and opinions of authors expressed herein do not necessarily state or reflect those of the United States Government or any agency thereof.

Nuclear Energy and Fuel Cycle Division

**METHODS FOR ESTIMATING DOSE FROM GALACTIC COSMIC RAYS AND  
JOVIAN RADIATION BELTS ON REDUCED-ORDER MONTE CARLO  
GEOMETRIES**

Mathew W. Swinney  
Michael B. R. Smith

August 2021

Prepared by  
OAK RIDGE NATIONAL LABORATORY  
Oak Ridge, TN 37831-6283  
managed by  
UT-BATTELLE LLC  
for the  
US DEPARTMENT OF ENERGY  
under contract DE-AC05-00OR22725



## CONTENTS

ABSTRACT .....	1
1. RADIATION ANALYSIS METHODOLOGY .....	1
1.1 Source Terms .....	1
1.1.1 Galactic Cosmic Rays .....	1
1.1.2 Jovian Trapped Radiation Belts .....	3
1.2 Geometry Decomposition .....	5
1.3 Variance Reduction Methods .....	8
1.4 Verification and Validation .....	9
1.4.1 GCR Simulations .....	9
1.4.2 Jovian $e^-$ and $p^+$ Simulations .....	11
2. SENSITIVITY STUDIES .....	12
2.1 Target Size Study .....	12
2.2 Angular Sensitivity Study .....	15
3. SUMMARY .....	18
4. REFERENCES .....	19
Appendix A .....	i
Observations of Charged Particle Penetration Through Spacecraft Materials .....	i

## ABSTRACT

This document outlines the methods and tools developed to estimate dose rates from galactic cosmic rays and the trapped radiation belts surrounding Jupiter using Monte Carlo particle transport software. Furthermore, the techniques described here are specific for translating high-resolution MAVRIC models to analogous but lower resolution Monte Carlo N-Particle Transport (MCNP) code models to estimate charged particle effects on models originally developed to study neutral particles only. This capability was initially developed to predict doses to various components of dynamic radioisotope power systems for spaceflight applications, but the tools and methods can be easily applied to other problem geometries and expanded to other space radiation environments.

## 1. RADIATION ANALYSIS METHODOLOGY

This document describes methods originally implemented to estimate radiation exposure to dynamic radioisotope power systems (DRPS) under consideration during Phase 2 of the 2016 Research Opportunities in Space and Earth Sciences solicitation as part of the Integrated Product Team's review. Although some elements from the original analysis may be discussed here, a separate proprietary report describes those systems in detail, as well as the estimated doses to various components and recommendations based on the associated analysis. The methodology presented in this report is designed to model two primary ionizing radiation sources that spacecraft are likely to encounter during a variety of potential deep-space missions: the ever-present galactic cosmic ray (GCR) spectrum and the intense trapped radiation belts found around Jupiter. By comparing the calculated radiation exposures to empirically derived, radiation-induced degradation effects of materials, a radiation resistance of specific components can be estimated. Alternatively, the methods could be modified to provide estimates of equivalent dose to biological systems inside a spacecraft. This section details the source terms developed for the Monte Carlo radiation transport calculations, followed by the geometry decomposition used, the variance reduction techniques employed, and verification and validation efforts. The entire charged particle transport was conducted using the Monte Carlo N-Particle Version 6 (MCNP6) nuclear analysis code developed by Los Alamos National Laboratory [1].

### 1.1 SOURCE TERMS

#### 1.1.1 Galactic Cosmic Rays

GCRs represent an ever-present isotropic radiation field found throughout the universe resulting from supernovae and other stellar activity. The GCR spectrum is composed of high-energy ( $\sim 100$  keV – 10 GeV) ions ranging from hydrogen to uranium, but it has a relatively low particle flux ( $\sim 1$  particle/cm<sup>2</sup>/s). The elemental composition of the spectrum is heavily skewed toward the lighter elements:  $\sim 87\%$  hydrogen,  $\sim 12\%$  helium, and  $\sim 1\%$  other ions [2]. Figure 1 shows the relative abundances of the lightest (and most abundant) 28 GCR ions. This work used a semi-empirical model developed at the German Aerospace Center (DLR), which requires the single solar modulation parameter ( $W$ ) to describe energy-dependent, galactic cosmic ray intensities for ions  $Z = 1 - 28$  [2].

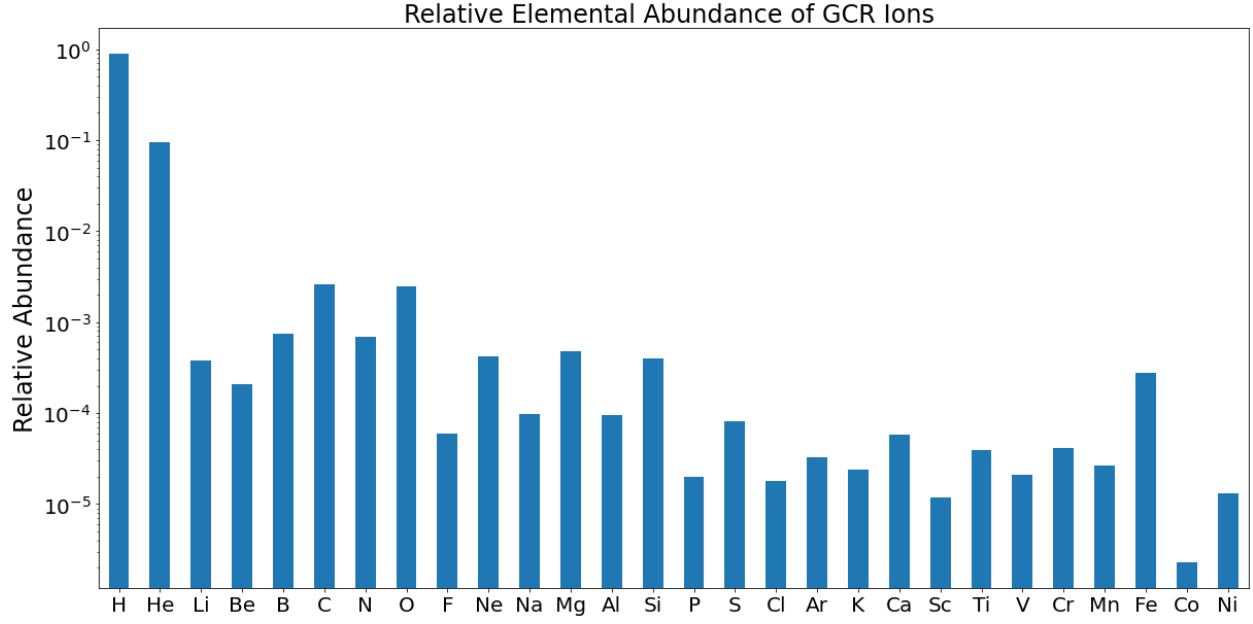


**Figure 1. Elemental abundances of GCR ions from hydrogen ( $Z = 1$ ) to nickel ( $Z = 28$ ).**

The intensity of the GCR spectrum is modulated by the heliosphere (the Sun's magnetic field) because some ions are deflected as a result of the electromagnetic interactions with the field. The modulation over time corresponds to the roughly 11 y solar cycle and is described by the parameter  $W$ , which can be directly correlated to the International Sunspot Number, terrestrial surface neutron monitors ( $W_{\text{Oulu}}$ ), or particle flux measurements from the Advanced Composition Explorer (ACE) satellite ( $W_{\text{ACE}}$ ). A tool called GCR SpecGen (based on DLR's GCR model) was used to create the source terms in this work [3]. An example of the GCR SpecGen window used for visualizing  $W$  and an example of the modulation effects on hydrogen are shown in Figure 2.  $W$  can be correlated to GCR SpecGen, which allows the user to select  $W$  based on historic values (specified by a date) or by explicitly entering a  $W$  value to generate the appropriate spectra for each of the GCR ions.

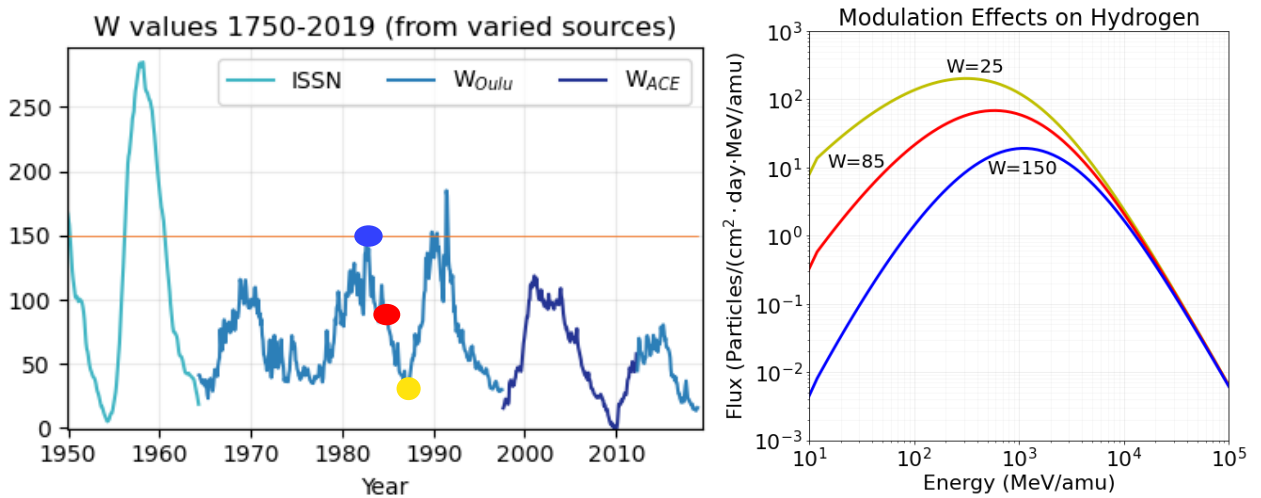


**Figure 2. GCR Modulation Parameter (left),  $W$ , which captures the effect of the solar modulation on the GCR spectrum (right). Images created using GCR SpecGen.**

To capture the dose contributions from the various ions that make up the GCR spectrum, 28 separate MCNP6 simulations were performed from  $Z = 1$  (hydrogen) to  $Z = 28$  (nickel). For example, a modulation parameter ( $W = 50$ ) based on an average value of the past  $\sim 50$  y was assumed for this analysis, although it would be trivial to incorporate any solar modulation if a specific mission time period or modulation intensity were needed.

### 1.1.2 Jovian Trapped Radiation Belts

The radiation belts around Jupiter consist primarily of electrons ( $e^-$ ) and protons ( $p^+$ ) trapped by the planet's intense dipole-like magnetic fields. The energies range to over  $\sim 100$  MeV, and the average particle flux can range from  $10^4 - 10^8$  particles/cm<sup>2</sup>/s depending primarily on proximity to and location within Jupiter's magnetosphere.

Although trapped radiation belts found around other planets (i.e., Earth, Saturn, Uranus, and Neptune) represent a potentially significant source of exposure, Jupiter serves as a worst-case scenario (with a magnetic moment approximately 20,000 times that of the Earth) for trapped radiation environments. Therefore, Jupiter is a good bounding case.

In 1983, Divine and Garrett made the first attempt to model the Jovian environment by incorporating measurements from Pioneer (10 and 11) and Voyager (1 and 2) spacecraft, which will be referred to hereinafter as the DG model [4]. The DG model was based primarily on data returned by instruments on the Pioneer and Voyager spacecraft, supplemented by Earth-based observations and theoretical considerations. The model was constructed as a 14-parameter fit of electron (and proton) flux as a function of pitch angle and  $L$  shell. The  $L$  shell parameter describes a particular set of magnetic field lines that cross the magnetic equator of the planet at a distance equal to  $L$  times the planet's radius. Thus, at the magnetic equator, the  $L = 9$  R<sub>J</sub> shell is at a distance from the center of Jupiter equal to nine times its radius. The differential intensity predicted by the DG model in units of (cm<sup>2</sup> s sr MeV)<sup>-1</sup> is given by Eq. (1) (Eq. 9 in the paper by Divine and Garrett), where  $I$  is the integral intensity (in the reference, Eq. 8) and the coefficients (in the reference, Eq. 7) are calculated from the parameters given in the corresponding tables (in the reference, Table 4 for electrons and Table 5 for protons).

$$F_{DG}(E, L) = \left(\frac{I}{E}\right) \left[ A_1 + \frac{A_2 - A_1}{1 + (D_2/E)^2} + \frac{A_3 - A_2}{1 + (D_3/E)^3} \right]. \quad (1)$$

For this work, the DG model was adapted into a Python Jupyter notebook named JovianSpecGen (inspired by GCR SpecGen), in which input parameters are provided and formatted text files are generated for use in MCNP6 simulations. JovianSpecGen was verified by replicating the results from the original DG source accurately [4]. Figure 3 presents a set of proton fluxes generated with JovianSpecGen that replicates a very similar plot from the original DG paper. The electron model used in this work has been continuously updated and requires additional explanation.



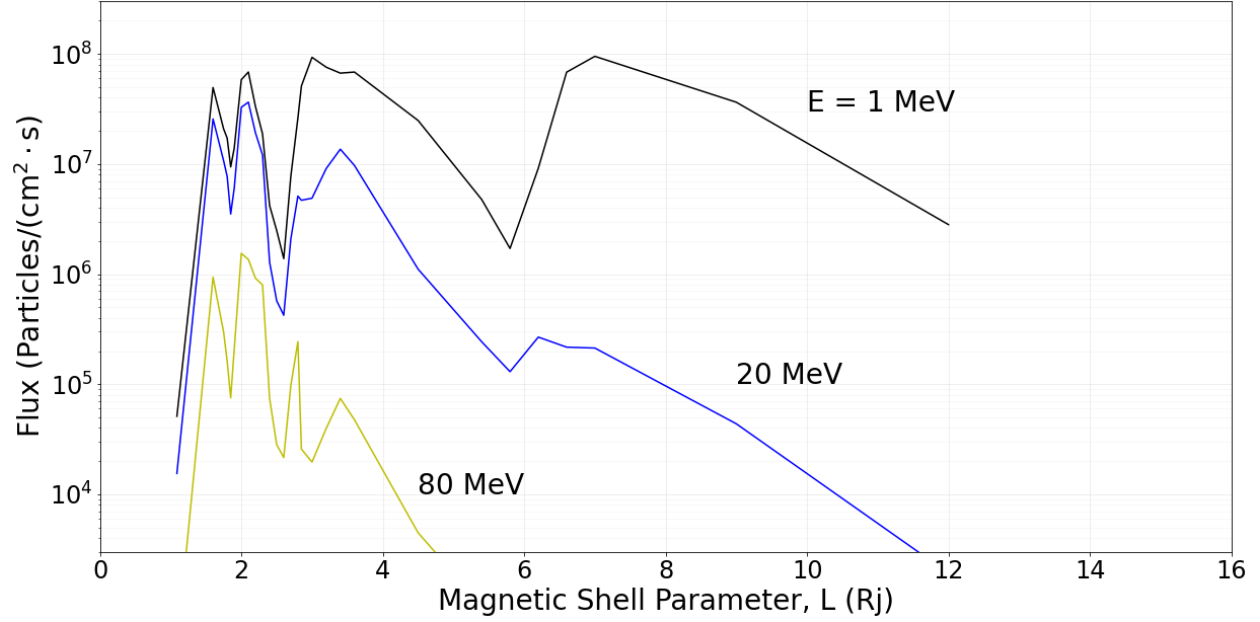


**Figure 3. Jupiter's integral proton fluxes as a function of L shell and energy generated by JovianSpecGen for comparison to Fig. 3 from the original DG model [4].**

The DG electron model has been periodically updated and modified primarily by personnel at the National Aeronautics and Space Administration (NASA) Jet Propulsion Laboratory to incorporate synchrotron radiation [5] and subsequent measurements from the Galileo mission [6]. The model used to create the source term for this work is referred to in the literature as the Galileo Interim Radiation Electron Model version-2 (GIRE2) [5].

GIRE2 is an empirical model that uses data sets obtained by the Galileo spacecraft to supplement the data-starved DG model. GIRE2 adopts the original DG model inside  $L < 8$ , and the region  $8 < L < 17$ , is based on the Galileo Energetic Particle Detector data. These 10 min data averages were used to construct a best fit estimate using a linear regression, resulting in the fitting parameters  $A(L)$  and  $B(L)$  given in Table 3 in the paper by de Soria-Santacruz [5]. The omnidirectional differential electron flux is shown in Eq. (2) as  $F_{in}$  in  $(\text{cm}^2 \text{ s sr keV})^{-1}$  as a function of energy and L shell,

$$F_{in}(E, L) = J_0(L) \left( \frac{E}{1 \text{ MeV}} \right)^{-A(L)} \left( 1 + \frac{E}{E_0(L)} \right)^{-B(L)}. \quad (2)$$

A smoothing function is given as Eq. (3), which demonstrates the GIRE2 model transition between  $L = 7.2 - 10.5$ .

$$F_2(E, L) = \frac{F_{in}(E, L)(L - 7.2)}{3.3} + \frac{F_{DG}(E, L)(10.5 - L)}{3.3}. \quad (3)$$

An example of the electron flux generated with JovianSpecGen to  $L = 17$  is shown in Figure 4, which is directly comparable to a plot from the original GIRE2 model.

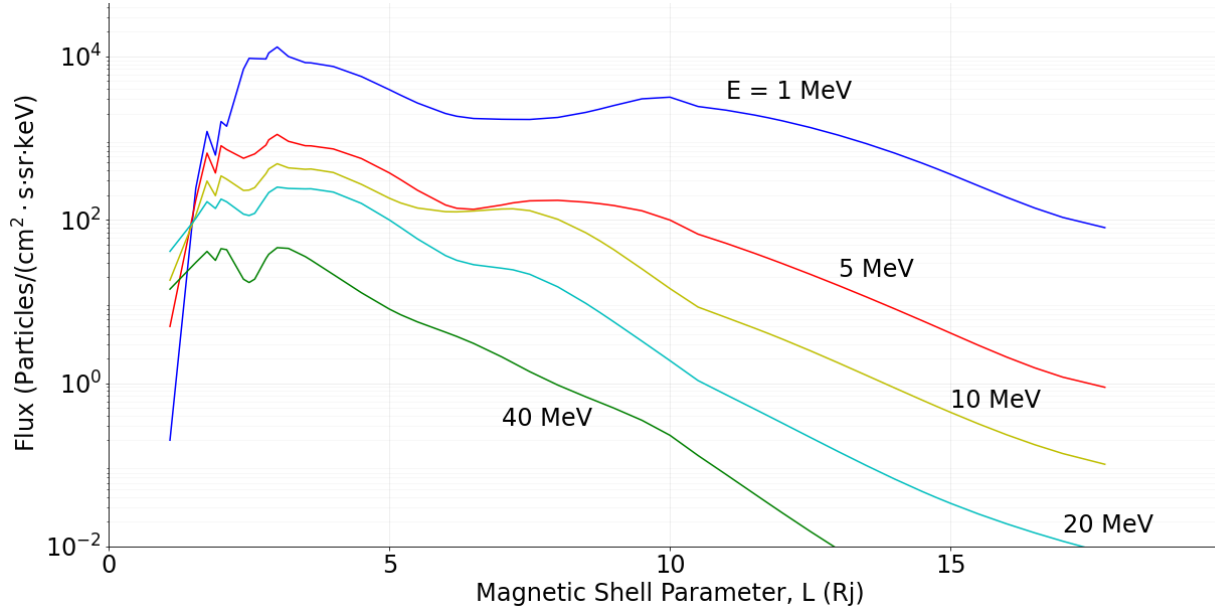


**Figure 4.** The differential electron flux at the magnetic equator generated by JovianSpecGen for comparison to Fig. 6 from the original GIRE2 model [5].

The JovianSpecGen tool allows the user to select a given Jovian L shell and then produces the associated electron and proton flux spectrum in the form of standard MCNP6 source definition syntax, allowing it to be incorporated easily into a full simulation input file. Two separate MCNP6 radiation transport calculations can then be performed on a given geometry to estimate the total or itemized contributions of protons and electrons in the radiation belts of Jupiter.

## 1.2 GEOMETRY DECOMPOSITION

As discussed previously, the methodology presented here was developed to estimate charged particle radiation exposure to DRPS on preexisting MAVRIC geometries [7]. High-resolution models of these systems were developed from 2D drawings and 3D CAD files into MAVRIC geometries. An example cross section of a high-resolution converter geometry is shown in Figure 5.

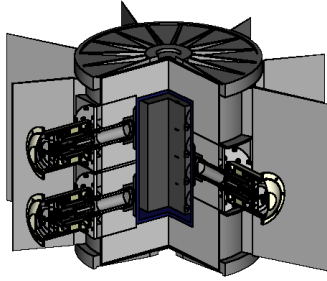


**Figure 5. Example of a high-resolution MAVRIC geometry to be simplified for MCNP6 charged particle simulations.**

Neutral particles (i.e., neutrons and photons) emanating from the radioisotope fuels were the original purpose of the high-resolution MAVRIC geometries. However, later investigations requested space radiation effects (i.e., charged particles), and the original geometries needed to be converted into a Monte Carlo code capable of transporting charged particles—MCNP6. Given the general isotropic behavior of space radiation and fundamental interactions of charged particles with matter, a lower resolution geometry approximation was deemed suitable to prevent recreating high-resolution models in two separate transport codes.

To achieve this, the charged particle calculations used a simplified geometry based on homogenized materials and binned areal densities ( $\text{g}/\text{cm}^2$ ) of the complex MAVRIC geometries. A ray-tracing tool was developed to interrogate the complex geometry by determining how much of the solid angle ( $4\pi$  view out from the component of interest) was occupied by some average areal density and material composition.

This technique takes a MAVRIC model and allows the user to select a component (or material) inside the geometry and perform an isotropic, reverse ray-tracing exercise from that location out through the greater geometry. Millions of particles are sampled in this way, and each individual ray trace catalogs its cumulative path length ( $L$ ) times the density of each material ( $\rho$ ), for every volume it transits. A single particle's path provides a single areal density value ( $\text{g}/\text{cm}^2$ ) over all transited volumes, and all the simulated particle paths are subsequently used to populate an areal density distribution. This distribution is then subdivided into eight equally spaced bins between the maximum and minimum areal densities. The areal densities and composition of each angular bin are represented as an equivalent solid angle in the simplified MCNP6 geometry, consisting of nested spheres cut by rotated planes to create equivalent solid angles. The source was an inward-directed, biased cosine source on a spherical surface that simulated an isotropic particle flux impinging on all sections of the shielding equally. The tally region at the center of the geometry represented the component of interest with a corresponding material composition. Ultimately, the MCNP6 geometry was represented as six nested spheres cut by three orthogonal planes, creating eight octants, each with five layers of shielding surrounding the target sphere at the center of the geometry. Each octant had a different areal density and composition, capturing the angular dependence of the shielding unique to each component investigated. Figure 6 illustrates the process of geometry decomposition.

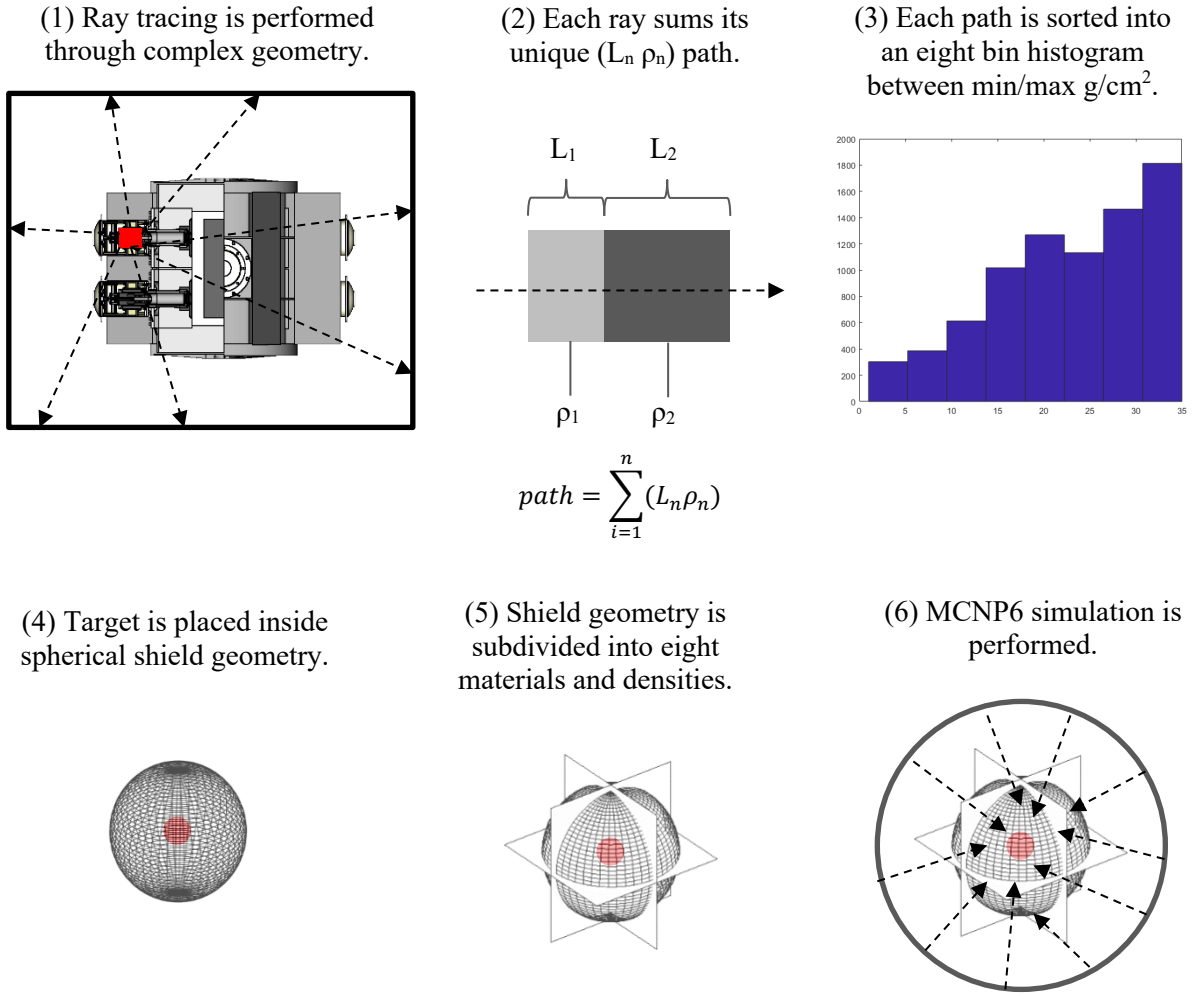


**Figure 6. Illustration of geometry decomposition sequence and methods.**

Table 1 provides an example of the mean areal densities calculated for different components in one of the DRPS systems. These mean areal densities represent the homogenized value for the shielding (i.e., the value that would be used if no attempt was made to capture the angular dependence of the shielding). Table 2 expands one of the entries in Table 1 (the polytetrafluoroethylene material) to illustrate the type of data used to capture the angular dependence of the shielding.

**Table 1. Example areal density data calculated from the DRPS model**

Material type	Mean areal density to component ( $g/cm^2$ )
Polytetrafluoroethylene (PTFE)	18.8
Polyimide (PI) Glass Fabric Laminate	15.0
Homogenized Cu, PI, and Epoxy	16.1
Glass Fabric Silicone Laminate	13.6
MoS <sub>2</sub> -Graphite-Polyimide	22.4
Diamethacrylate ester	10.2
Ethylene tetrafluoroethulene (ETFE)	14.4
SmCo Ceramic Permanent Magnets	22.7

**Table 2. Example areal densities for PTFE material with angular bins**

PTFE Areal Densities	
Bin	Thickness (g/cm <sup>2</sup> )
1	3.3
2	6.7
3	10.1
4	13.2
5	17.1
6	22.1
7	28.7
8	49.4
Avg.	18.8

After the angularly binned areal density of the shielding surrounding a component of interest was combined with the corresponding material composition of the shield, the simplified MCNP6 geometry could be completed, and the charged particle simulation could be performed.

### 1.3 VARIANCE REDUCTION METHODS

Although rigorous tools have been developed for optimizing Monte Carlo variance-reduction parameters for neutral particle transport [7], [8], they currently are not applicable to charged particles. Fortunately, the methodology discussed here implements a simplified geometry for the charged particle transport step, which lends itself well to leveraging standard variance reduction techniques. Four straightforward variance reduction strategies were implemented in these transport calculations: two based on biasing the source, one based on geometry splitting/rouletting, and one that utilized energy cutoffs within the problem geometry.

The source biasing took two forms: one form was based on the angular distribution of the particles emitted from the inwardly directed spherical surface, and the other was based on the sampling of the energy distribution. The angular biasing took on the form of a biased cosine, as shown in Figure 7 in the code snippet as ‘SB2’ in MCNP6 syntax, resulting in particles being preferentially directed toward the center of the problem geometry, where they can contribute to dose in the target. The sampling of the energy distribution was critical in these calculations because the Jovian electron and proton sources are heavily weighted toward the low-energy part of the spectrum. A straightforward sampling would waste substantial time simulating low-energy particles with a low probability of depositing energy in the target. Therefore, by forcing equal sampling from each of the bins and weighing the results appropriately (based on the source distribution), the calculation can spend more time transporting the higher energy particles that are more likely to contribute to dose in the target. This even sampling method is **bolded** in the MCNP6 code snippet below as SB1, biasing the energy distribution to sample from each energy bin equally (Figure 7).

```
c Source definition
SDEF PAR=E ERG=D1 SUR=999 NRM = -1 DIR=D2 WGT=5.458635E+12
SB1      0 1 98r
SB2  -21 2
```

**Figure 7. MCNP6 input example for uniform source sampling indicated by the SB1 card.**

The geometry-based variance reduction took the form of importance biasing, weighting particles closer to the target more than those near the periphery. This is shown in Figure 8 in the code snippet in **bold**. The example geometry is a simple set of nested spheres, in which the importance at the silicon target (the inner most sphere) is the highest (i.e., 64) and steadily decreases as the geometry progresses out farther from the center (i.e., 32, 16, 8, 4, 2, 1).

```

c Cells
1 1 -1.5 -1 IMP:n,p,e,h=64 $ Si Target
11 11 -2.6850 1 -2 IMP:n,p,e,h=32 $ Shielding
21 11 -2.6850 2 -3 ELPT:E=0.219 ELPT:H=5.809 IMP:n,p,e,h=16 $ Shielding
31 11 -2.6850 3 -4 ELPT:E=0.672 ELPT:H=14.731 IMP:n,p,e,h=08 $ Shielding
41 11 -2.6850 4 -5 ELPT:E=2.078 ELPT:H=31.277 IMP:n,p,e,h=04 $ Shielding
51 11 -2.6850 5 -6 ELPT:E=6.503 ELPT:H=59.225 IMP:n,p,e,h=02 $ Shielding
99 0 6 -999 ELPT:E=26.98 ELPT:H=117.47 IMP:n,p,e,h=01 $ Void
100 0 999 IMP:n,p,e,h=00 $ Graveyard

c Surfaces
1 SO 0.025 $ Surface of target material
2 SO 0.05 $ Surface of shielding
3 SO 0.15 $ Surface of shielding
4 SO 0.50 $ Surface of shielding
5 SO 1.50 $ Surface of shielding
6 SO 5.00 $ Surface of shielding
999 SO 50 $ Surface of void region

```

Figure 8. MCNP6 input example for uniform source sampling indicated by the SB1 card.

The final variance-reduction strategy was based on energy cutoffs within the geometry. The strategy focused on eliminating particles that could not physically reach the tally region based on known ranges of charged particles and the remaining amount of shielding to transit to the target. An example is shown as the underlined sections in the code snippet in Figure 8, in MCNP6 syntax. These values are based on the problem geometry, and the energy was chosen such that the range of the given particle ( $e^-$  and  $p^+$ ) at that energy equaled the shielding remaining interior to the current layer of the geometry. In other words, particles with less energy than the cutoff value have a range that is less than the amount of shielding remaining to the target. Therefore, they would have a negligible impact on the dose in the target material and were thus eliminated from the problem at that point.

## 1.4 VERIFICATION AND VALIDATION

### 1.4.1 GCR Simulations

The primary verification of the GCR simulations used in this work utilized a tool developed by NASA called the *On-line Tool for the Assessment of Radiation in Space* (OLTARIS) [9]. The transport and physics for this tool are based on the HZETRN and NUCFRG [10], [11] research codes, and it offers several potential GCR models, including the Matthia 2013 model used in this work (also used by GCR SpecGen) [1]. The first verification step was to ensure that GCR SpecGen could replicate the same source term for GCR in free space that OLTARIS produced, as shown in Figure 9.

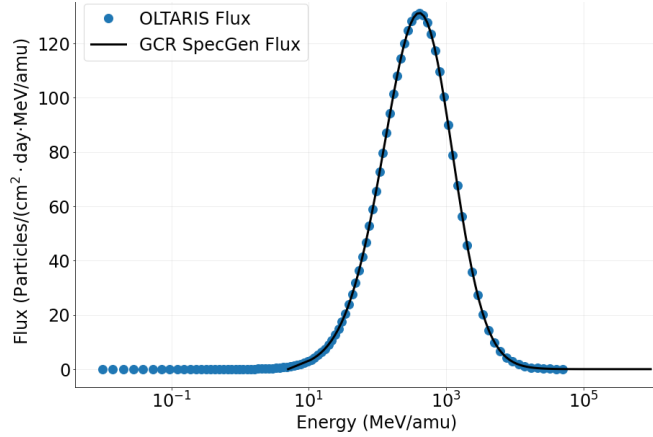


**Figure 9. Comparison of the GCR flux produced by OLTARIS to that created by GCR SpecGen for the hydrogen component ( $Z = 1$ ) of the GCR model presented by Matthiä. Similar plots were created for all the elemental components up to nickel ( $Z = 28$ ).**

Once the source terms between the two tools were confirmed to agree, both were used to estimate the dose in silicon behind several shielding thicknesses of aluminum. These results are shown in Table 3, which compares the OLTARIS results to those obtained with MCNP6.

**Table 3. Verification results comparing the dose rates predicted by OLTARIS vs. MCNP6 in a silicon target behind aluminum shielding**

Shield thickness (g/cm <sup>2</sup> )	Dose rate (OLTARIS) (mGy/day)	Dose rate (MCNP6) (mGy/day)	Ratio
0	0.25049	$0.2487 \pm 0.0009$	0.99
1	0.27304	$0.2785 \pm 0.0009$	1.02
5	0.28064	$0.2932 \pm 0.0009$	1.04

Validation of the GCR simulation methodology involved the comparison of dose rates obtained by the Radiation Assessment Detector (RAD) aboard the Mars Science Laboratory spacecraft during its transit to Mars. During quiet periods in solar activity, the average GCR dose rate measured was reportedly  $332 \pm 23$   $\mu$ Gy/day [12]. The RAD operated between December 6, 2011, and July 14, 2012. Using these dates in the GCR SpecGen tool yielded an average solar modulation value  $W$  of  $\sim 54$ , based on Oulu neutron monitor data [13]. This information was used to create the source term for the GCR validation simulations.

The shielding around the RAD instrument was complex, and most of the solid angle was lightly shielded with a density less than  $\sim 10$  g/cm<sup>2</sup>, but the density of other parts ranged up to  $\sim 100$  g/cm<sup>2</sup> [12]. To capture this range of shielding values, two simulations were completed: one with a layer of aluminum shielding equal to 5 g/cm<sup>2</sup> and another with a 30 g/cm<sup>2</sup> layer. The former case yielded a dose rate of  $300 \pm 6$   $\mu$ Gy/day, and the latter estimated a dose rate of  $328 \pm 16$   $\mu$ Gy/day. Because there was limited information about the exact angular distribution of the areal densities surrounding the RAD detector and an average areal density of 30 g/cm<sup>2</sup> was assumed, the dose rate was within the measured uncertainties, as shown in Table 4.

<b>Table 4. Validation results comparing RAD detector measurements to two MCNP6 simulations</b>			
	RAD measurement	MCNP6 simulation 1	MCNP6 simulation 2
Dose rate ( $\mu\text{Gy/day}$ )	$332 \pm 23$	$300 \pm 6$	$328 \pm 16$
Areal density ( $\text{g/cm}^2$ )	$5 < (\text{g/cm}^2) > 100$	5	30

### 1.4.2 Jovian $e^-$ and $p^+$ Simulations

Aside from the verification previously discussed during the development of the JovianSpecGen tool, additional verification was performed by comparing dose rates estimated by Moscow State University and the Russian Academy of Sciences [14]. In this paper, radiation conditions in Jupiter’s environment are estimated, and particular attention is given to doses in the orbit of Europa, one of Jupiter’s moons. The authors were interested in estimating the dose behind various amounts of shielding over the course of a 2-month mission in an orbit near Europa. This scenario was replicated using JovianSpecGen to select an orbit of  $9.5 R_J$  to create the source term, and MCNP6 was used to compute the dose rate behind the shielding configurations. Then, the results over 2 months were integrated to produce figures that could be directly compared to the results presented in the paper by Podzolko et al [14]. This comparison is presented in Table 5.

<b>Table 5. Comparison of total estimated dose for two months in the orbit of Europa</b>			
Shield Thickness ( $\text{g/cm}^2$ )	Dose (Podzolko) (rad)	Dose (this work) (rad)	Ratio
0.0	$8.50\text{E} + 08$	$7.62\text{E} + 08$	0.90
0.1	$1.50\text{E} + 07$	$1.44\text{E} + 07$	0.96
1.0	$2.20\text{E} + 06$	$2.36\text{E} + 06$	1.07
5.0	$2.40\text{E} + 05$	$2.48\text{E} + 05$	1.03
10.0	$4.50\text{E} + 04$	$4.65\text{E} + 04$	1.03

Podzolko et al. showed the strong dependence of dose from electrons and protons, even on relatively small amounts of shielding; protons contributed significantly only below  $0.1 \text{ g/cm}^2$  (shown in Figure 10).



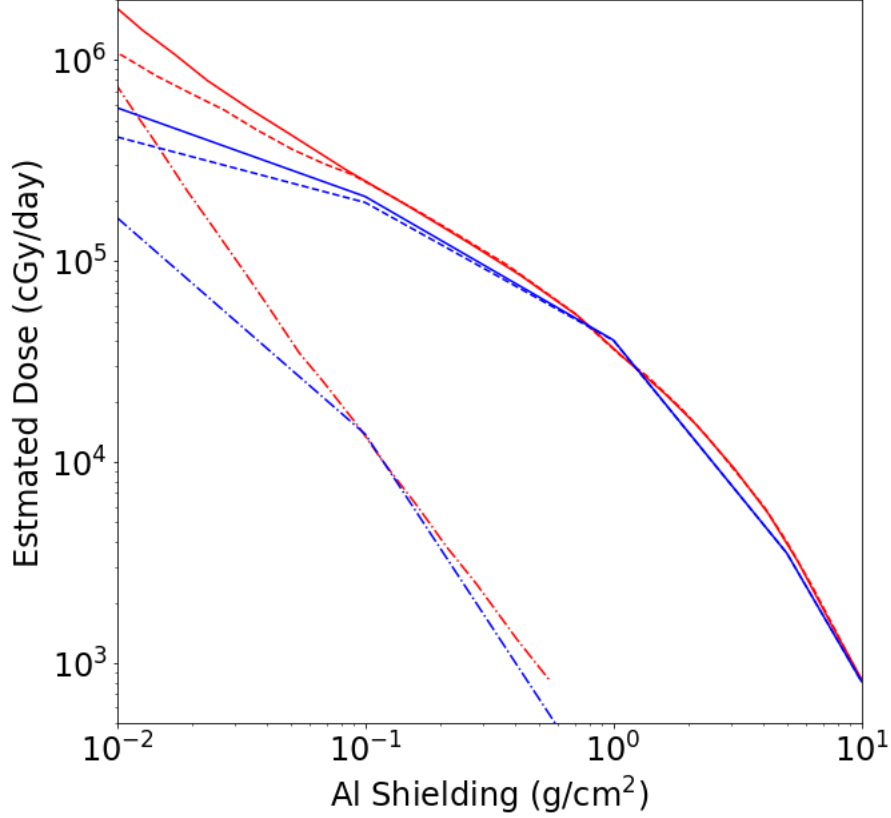
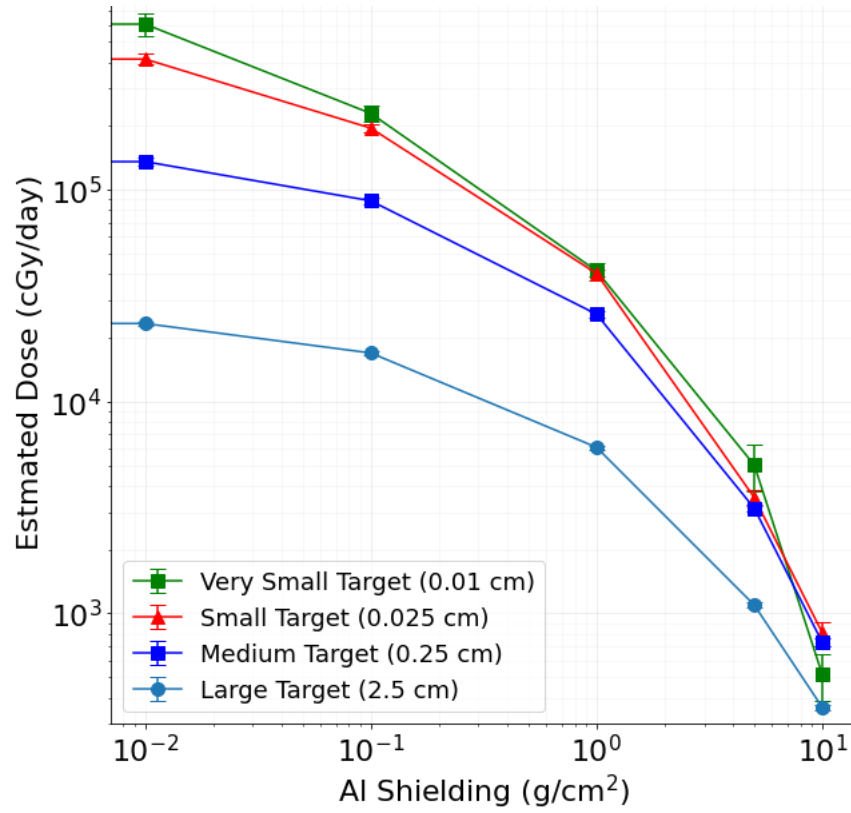


**Figure 10.** Estimated radiation doses behind different shield thicknesses from electrons (dash), protons (dot-dash), and the total (solid). Results from this work are in blue, compared to Podzolk et al. (red).

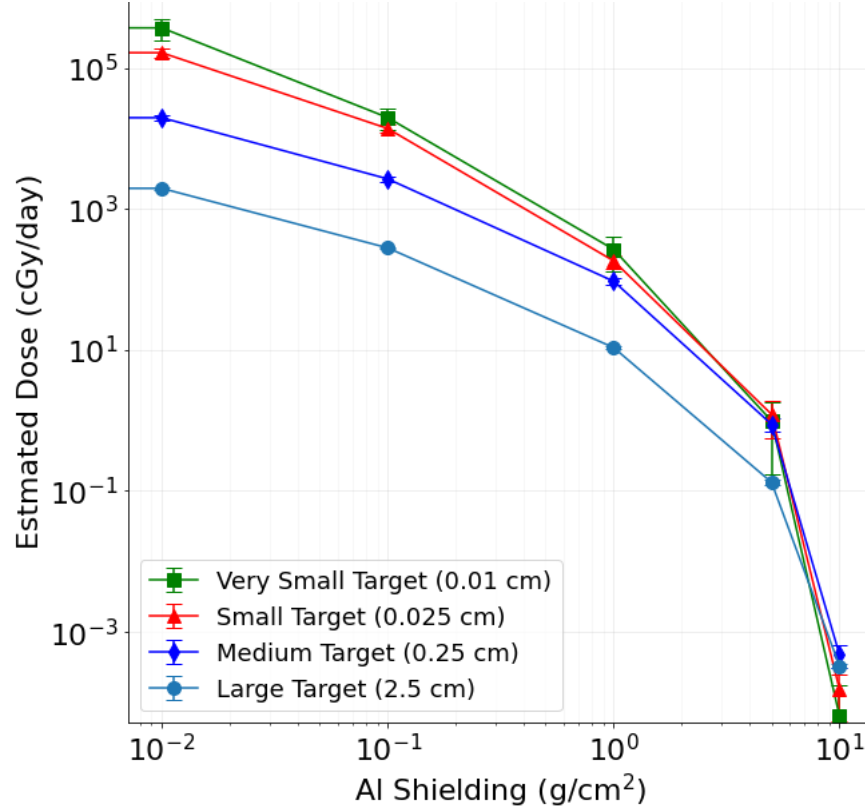
## 2. SENSITIVITY STUDIES

### 2.1 TARGET SIZE STUDY

One of the primary concerns related to the relatively simple geometry utilized in this work was how to best size the target material. The size of the target at the center of the nested spheres had to interact with the incident particle field but not more than the actual component under investigation would have. Also, the volume of the target had to be large enough to generate statistically sound results in an acceptable time frame yet not produce nonphysical geometric effects that the actual component would not induce. To understand the effect of target size on the dose estimate, four target sizes were chosen with radii of 0.01, 0.025, 0.25, and 2.5 cm and simulated behind various amounts of aluminum shielding. The largest of these was chosen specifically to be an extreme case meant to exaggerate the effect of the target size on the dose estimate. These results are shown in Figure 11 for trapped electrons and Figure 12 for trapped protons.



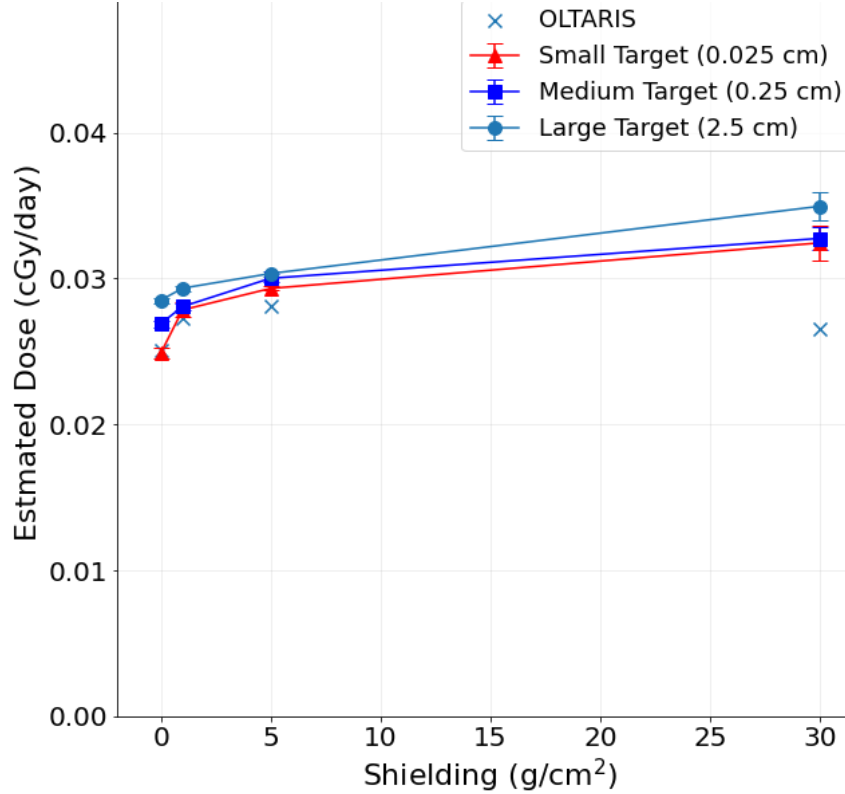
**Figure 11. Estimated dose from the Jovian electron source in a silicon target of varying radii behind different amounts of aluminum shielding.**



**Figure 12. Estimated dose from the Jovian proton source in a silicon target of varying radii behind different amounts of aluminum shielding.**

The results for these two cases suggest that there is a misleading and significant reduction in the estimated dose in the target for the large target but that the effect was still relatively important for the medium target. It is assumed that one of the primary phenomena causing this effect is a form of self-shielding, where dose at the edge of the target is significantly higher than that at the center. Unless the target component is thick enough to display this sort of behavior, then incorporating this artifact into the simulations is highly undesirable, and a smaller target should be chosen. The effect appears to be less significant when more shielding is present, which is consistent with expectations because the lower energy component is screened out before reaching the target, and the more energetic electrons and protons reaching the target are less sensitive to the size of the target material.

A similar study was conducted with the GCR source term, as shown in Figure 9. Here the impact is significantly less noticeable than in the electron and proton case, but it should be noted that a small target was still necessary to match the non-shielded OLTARIS results precisely. The deviation from OLTARIS as the level of shielding increases is in part caused by some simplifying assumptions made by the models used by OLTARIS, for which the 3D features of coupled nucleon transport are not treated in full detail, as discussed by Slaba et al. [15]. The y axis plotted in Figure 12 overemphasizes the effect of the target size and the discrepancy among simulations, as the difference in dose is relatively small for all the presented results. Doses from GCR are largely insensitive to moderate shielding and target material.

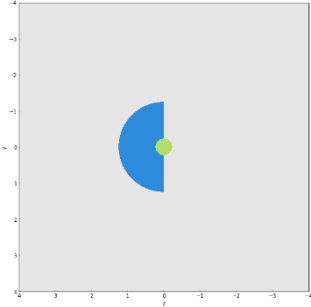
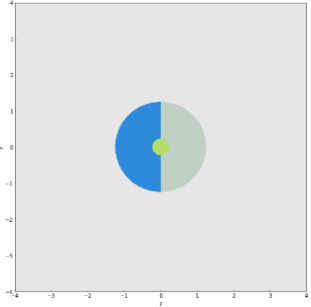
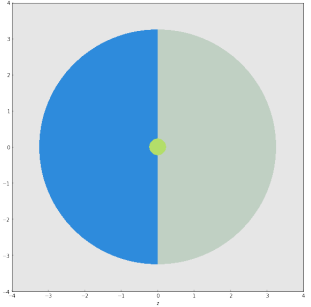


**Figure 12. Estimated dose from the GCR source in a silicon target of varying radii behind different amounts of aluminum shielding.**

## 2.2 ANGULAR SENSITIVITY STUDY

An analysis was conducted to investigate the impact of homogenizing shielding that is innately heterogenous to understand some of the uncertainties incurred during the geometry simplification process. Table 6 describes three separate cases used to examine the effect on the estimated dose to a small silicon target when two dissimilar hemispheres of shielding are homogenized. The first case defined half of the solid angle of the target shielded with water, and the other half was left unshielded. The second and third cases had water shielding  $2\pi$  steradians (i.e., half) and aluminum shielding the other  $2\pi$ , at different areal densities. To avoid unintended geometric artifacts resulting from different physical shielding thicknesses, the thickness was made consistent for each hemisphere, and the density of the material was modified to maintain the areal density.

**Table 6. Description of angular homogenization cases**

Case	spheres_02	spheres_03	spheres_04
2D cross section			
Shield thickness	1 cm	1 cm	3 cm
Material	Water and vacuum	Water and Al	Water and Al
Angular areal density	1 g/cm <sup>2</sup> and 0 g/cm <sup>2</sup>	1 g/cm <sup>2</sup> and 3 g/cm <sup>2</sup>	1 g/cm <sup>2</sup> and 9 g/cm <sup>2</sup>
Homogenized areal density	0.5 g/cm <sup>2</sup>	2 g/cm <sup>2</sup>	5 g/cm <sup>2</sup>

For this study, a GCR source with an average solar modulation was used ( $w \sim 50$ ), as well as an electron and proton source representative of the trapped radiation belts around Jupiter, near the orbit of Europa ( $\sim 9.5 R_j$ ).

The results were extremely different for the two source spectra investigated (GCR and Jovian radiation belts), as indicated in Tables 7 and 8. The effect of homogenization on the estimated dose from the GCR source was minimal. This result supports previously published conclusions describing that dose contributions from GCR are relatively insensitive to shielding [15]. In stark contrast, the effect of homogenizing the shielding for the Jovian trapped electrons and protons was significant. This result was expected because both protons and electrons of the energies found in the belts around Jupiter have relatively short ranges in common shielding materials. Although the effect can be extreme for protons, they are not a major contributor to dose for shielding above  $\sim 0.1 \text{ g/cm}^2$ , as shown in Figure 10. Based on this narrow study, a gross homogenization of shielding could result in an underprediction of dose by a factor of 2–4 or even more. This would be highly dependent on how heterogenous the shielding is in practice, but this exercise provides an example of how this methodology could underestimate dose in highly heterogenous shielding configurations.

**Table 7. GCR angular results**

Case	Angular dose (cGy/day)	Homogenized dose (cGy/day)	H/A
spheres_02	$(2.71 \pm 0.03) \times 10^{-2}$	$(2.71 \pm 0.03) \times 10^{-2}$	0.998
spheres_03	$(2.76 \pm 0.03) \times 10^{-2}$	$(2.77 \pm 0.04) \times 10^{-2}$	1.002
spheres_04	$(2.73 \pm 0.03) \times 10^{-2}$	$(2.86 \pm 0.03) \times 10^{-2}$	1.046

<b>Table 8. Jovian angular results</b>			
Case	Angular dose (cGy/day)	Homogenized dose (cGy/day)	H/A
<b>Protons</b>			
spheres_02	$(3.54 \pm 0.07) \times 10^4$	$(2.58 \pm 0.11) \times 10^2$	0.007
spheres_03	$(3.56 \pm 0.26) \times 10^1$	$(1.80 \pm 0.18) \times 10^1$	0.504
spheres_04	$(3.20 \pm 0.23) \times 10^1$	$(1.18 \pm 0.32) \times 10^0$	0.037
<b>Electrons</b>			
spheres_02	$(1.01 \pm 0.03) \times 10^5$	$(4.56 \pm 0.08) \times 10^4$	0.452
spheres_03	$(1.64 \pm 0.04) \times 10^4$	$(1.27 \pm 0.03) \times 10^4$	0.775
spheres_04	$(1.30 \pm 0.03) \times 10^4$	$(3.71 \pm 0.18) \times 10^3$	0.285

A second study was conducted to investigate the importance of accurately capturing the angular dependence of the shielding surrounding a point of interest. The set of simulations therein was designed to capture the effect of binning the shielding into various numbers of equally sized angular bins, focusing on an extremely heterogenous case. These cases are shown in Table 9, giving the mean areal density calculated for each of the bins as a function of the total number of bins. The mean areal density remained constant at  $6.202 \text{ g/cm}^2$ ; however, as the final entry demonstrates, a single angular bin (i.e.,  $4\pi/8 = \sim 1.57$  steradians) contains most of the shielding mass. The estimated dose in a silicon target for six of these different shielding cases was computed, and the results are shown in Figure 13 for both protons and electrons. From these results, it was determined that using at least four bins is necessary to avoid significant errors, but simulations with eight bins should be more than capable of capturing most of the heterogeneity present, even in this extreme case.

<b>Table 9. Extreme angular case study of shielding configurations</b>								
<b>(units of mean areal density in <math>\text{g/cm}^2</math>)</b>								
<b>Bin no.</b>	<b>1 Bin</b>	<b>2 Bins</b>	<b>3 Bins</b>	<b>4 Bins</b>	<b>5 Bins</b>	<b>6 Bins</b>	<b>7 Bins</b>	<b>8 Bins</b>
1	6.202	1.132	1.072	1.037	1.012	0.994	0.982	0.973
2		11.273	1.281	1.227	1.184	1.15	1.123	1.1
3			16.254	1.41	1.286	1.251	1.219	1.192
4				21.135	1.567	1.31	1.288	1.262
5					25.963	1.932	1.393	1.307
6						30.576	2.660	1.515
7							34.751	3.557
8								38.713
Avg.	6.202	6.203	6.202	6.202	6.202	6.202	6.202	6.202

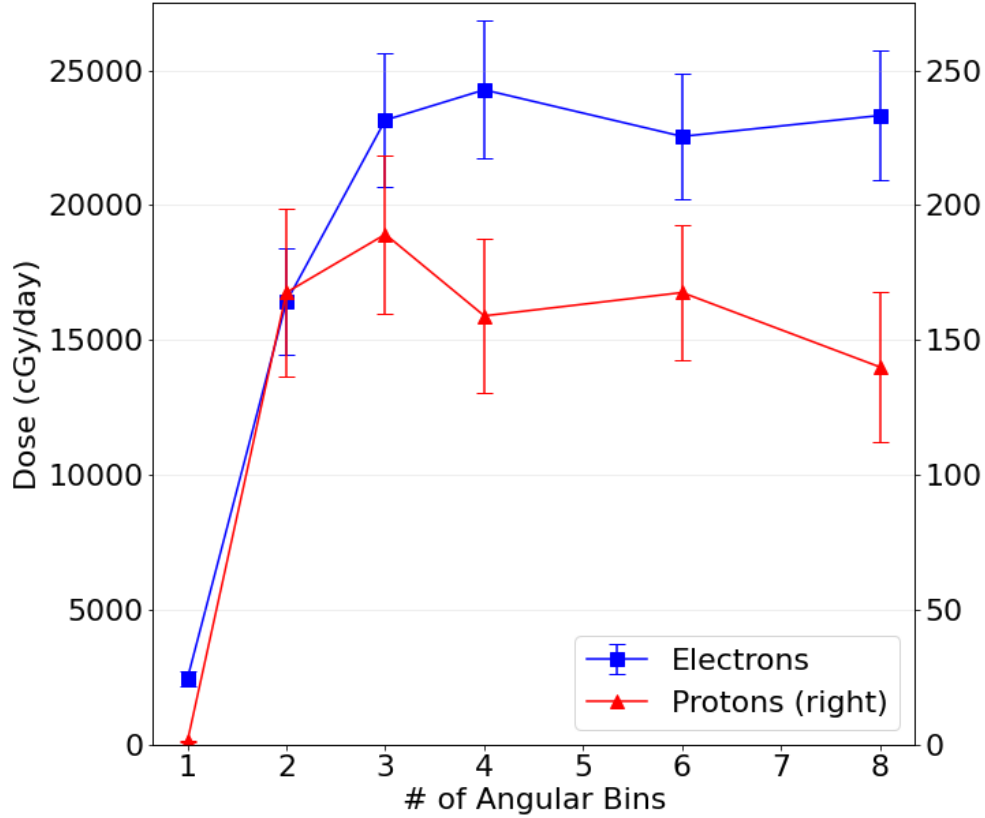


**Figure 13. Results from extreme angular case study, corresponding to cases described in Table 9.** A highly heterogeneous shielding configuration is homogenized over a different number of angular bins, and the resulting estimated dose from electrons and protons is presented.

### 3. SUMMARY

This report describes methods to convert complex radiation transport geometries from MAVRIC into simplified MCNP6 geometries for charged particle simulations. These methods were developed in support of analysis of DRPS components subjected to mixed radiation fields emanating from (1)  $\text{PuO}_2$  and (2) natural space radiation. If a high-resolution geometry is created (or exists) in a transport code capable of simulating neutral and charged particles, then these methods are not necessary. However, if a geometry (that is time-prohibitive to recreate) exists in a code that only supports neutral particle transport (i.e., SCALE), then the methods described in this work can serve as a method for efficiently and accurately estimating charged particle radiation exposures commonly encountered during spaceflight scenarios. These geometry decomposition methods were validated and verified to recreate a reduced-order analog to the high-resolution original geometries.

#### 4. REFERENCES

- [1] Werner, C. J., et al. 2018. “MCNP User’s Manual.”, Los Alamos National Security, LLC. LA-UR-17-29981
- [2] Matthiä, D., et al. 2013. “A Ready-to-Use Galactic Cosmic Ray Model,” *Adv. Space Res* 51(300), 329–338. <https://doi.org/10.1016/j.asr.2012.09.022>.
- [3] Ratliff, H. 2019. “Lindt8/GCR\_SpecGen: GCR-SpecGen release v1.0,” *Lindt8/GCR\_SpecGen: GCR-SpecGen release v1.0*. <https://doi.org/10.5281/zenodo.2573360>.
- [4] Divine, N., and H. B. Garrett. 1983. “Charged Particle Distributions in Jupiter’s Magnetosphere,” *J. Geophys. Res. Space Phys.* 88(A90, 6889–6903. <https://doi.org/10.1029/JA088iA09p06889>.
- [5] de Soria-Santacruz, M., et al. Oct. 2016. “An Empirical Model of the High-Energy Electron Environment at Jupiter: GIRE2 Jovian Radiation Model,” *J. Geophys. Res. Space Phys.* 121(10), 9732–9743. <https://doi.org/10.1002/2016JA023059>.
- [6] Garrett, H. B., R. Evans, and W. Kim. Aug. 2015. “Updating the Jovian Plasma and Radiation Environments—The Latest Results for 2015,” AIAA SPACE 2015 Conference and Exposition. <https://doi.org/10.2514/6.2015-4556>.
- [7] D.E. Peplow. May 2011. “Monte Carlo Shielding Analysis Capabilities with MAVRIC,” *Nucl. Technol.* 174. <https://web.ornl.gov/~peplowde/p049.pdf>.
- [8] Mosher, S. W., et al. 2013. “ADVANTG – An Automated Variance Reduction Parameter Generator,” Oak Ridge National Laboratory, ORNL/TM-2013/416. <https://info.ornl.gov/sites/publications/files/Pub46035.pdf>.
- [9] Singleterry, R. C., et al. 2011. “OLTARIS: On-line tool for the assessment of radiation in space,” *Acta Astronaut.* 68(7), 1086–1097. <https://doi.org/10.1016/j.actaastro.2010.09.022>.
- [10] Wilson, J. W., et al. 1991. “HZETRN: a heavy ion/nucleon transport code for space radiations.”
- [11] Townsend, J. W. and J. W. Wilson. 1987. “An Algorithm for a Semiempirical Nuclear Fragmentation Model,” *Comput. Phys. Commun.* 47, 81–294.
- [12] Guo, J., et al. 2015. “Variations of Dose Rate Observed by MSL/RAD in Transit to Mars,” *Astron. Astrophys.* 577, A58.
- [13] “Cosmic Ray Station of the University of Oulu.” Neutron Monitor Database. <http://cosmicrays.oulu.fi/>.
- [14] Podzolko, M. V., et al. April 2009. “Radiation conditions of a mission to Jupiter and Europa,” *Sol. Syst. Res.* 43( 2), 116–120. <https://doi.org/10.1134/S0038094609020038>.
- [15] Slaba, T. C., et al. Feb. 2017. “Optimal Shielding Thickness for Galactic Cosmic Ray Environments,” *Life Sci. Space Res.* 12, 1–15. <https://doi.org/10.1016/j.lssr.2016.12.003>.





## APPENDIX A

### OBSERVATIONS OF CHARGED PARTICLE PENETRATION THROUGH SPACECRAFT MATERIALS

During this investigation, much time was spent comparing ranges of charged particles in different materials, and these relationships were studied in multiple radiation environments (i.e., GCR, and Jovian belts) over many orders of magnitude in energy. Trying to reconcile these various relationships in a workable format drove the visual coupling of a given source spectrum's average range to a given bulk material's shielding effectiveness.

The following plots represent various threshold areal densities (red dashed lines) and serve as an integrating demarcation for spectral energies that will contribute to absorbed dose.

For example, Figure A1 shows the energy-dependent electron spectrum at 9.5 R<sub>j</sub> (i.e., approximately Europa's orbital radii) as indicated by the blue line. The first red dashed line on the left of the figure represents the spectral cutoff for 0.01 g/cm<sup>2</sup>, where every particle energy to the left of this line does not contribute to the ~440 krad/day but everything to the right of this line does contribute. Conversely, the far-right red dashed line for 10 g/cm<sup>2</sup> indicates that only electrons >~20 MeV contribute to the internally shielded ~1 krad/day, and all energies to the left do not.

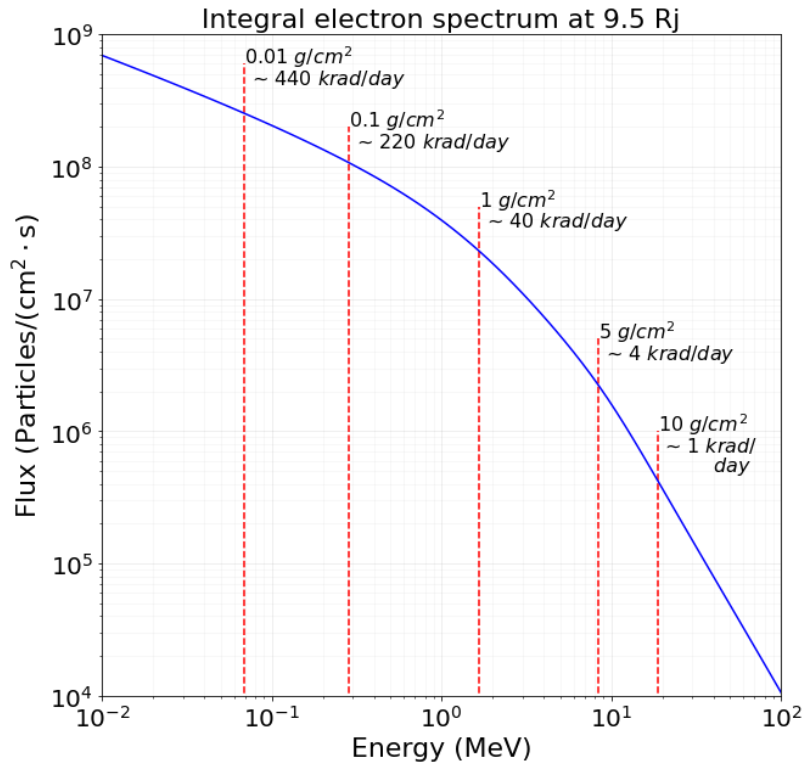


**Figure A1: Integral electron spectrum assumed near Europa's orbit (9.5 R<sub>j</sub>) for the presented analysis. The red-hashed line represents the electron energy corresponding to the range (in Al) shown at the top. The dose-rate represents an estimate of the dose-rate (in Si) behind an aluminum shield of the listed thickness.**

This same relationship was plotted for the proton fields around Jupiter at the 9.5 R<sub>J</sub> (Figure 15). Because of the comparatively shorter range of protons (when compared to the same energy of electron), the relationships presented on Figure A2 are compressed into only two decades of energy where the previous plot for electrons spanned four decades. For example, 10 g/cm<sup>2</sup> of shielding for electrons allows energies more than ~20 MeV to contribute to the ~1 krad/day expected absorbed doses. Conversely, 10 g/cm<sup>2</sup> of shielding reduces the entire Jovian proton spectrum to energies more than ~100 MeV (i.e., the vast minority of the proton energy spectrum) and a resulting ~0.2 rad/day. Lower energy charged particles carry a higher linear energy transfer (LET) and higher LET particles impart higher absorbed doses.

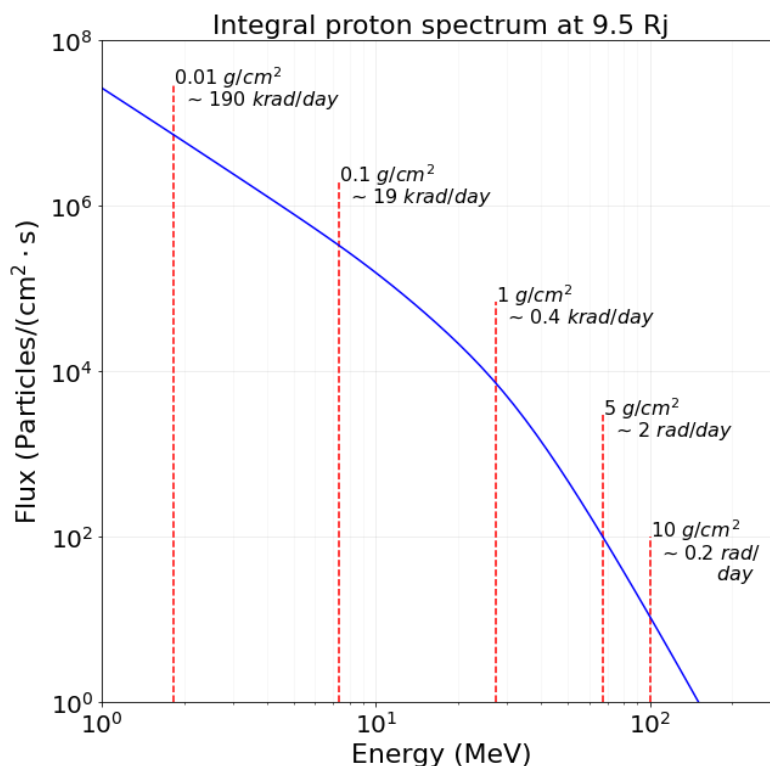


**Figure A2: Integral proton spectrum assumed near Europa's orbit (9.5 R<sub>J</sub>) for the presented analysis. The red-hashed lines represent the proton energy corresponding to the range (in Al) shown at the top. The dose-rate represents an estimate of the dose-rate (in Si) behind an aluminum shield of the listed thickness.**

Figure A3 shows the same relationships of charged particles and range superimposed on an average modulated proton portion of the GCR spectrum at average modulation ( $W \sim 50$ ). Because of the comparatively high energies observed in GCRs, only the lowest energies of the spectrum ( $< \sim 200$  MeV/n) are affected by significant amounts of shielding. Regardless, visually tying these shielding thicknesses to dose rates and to spectral energies was an informative exercise while honing engineering decisions involved with this analysis.

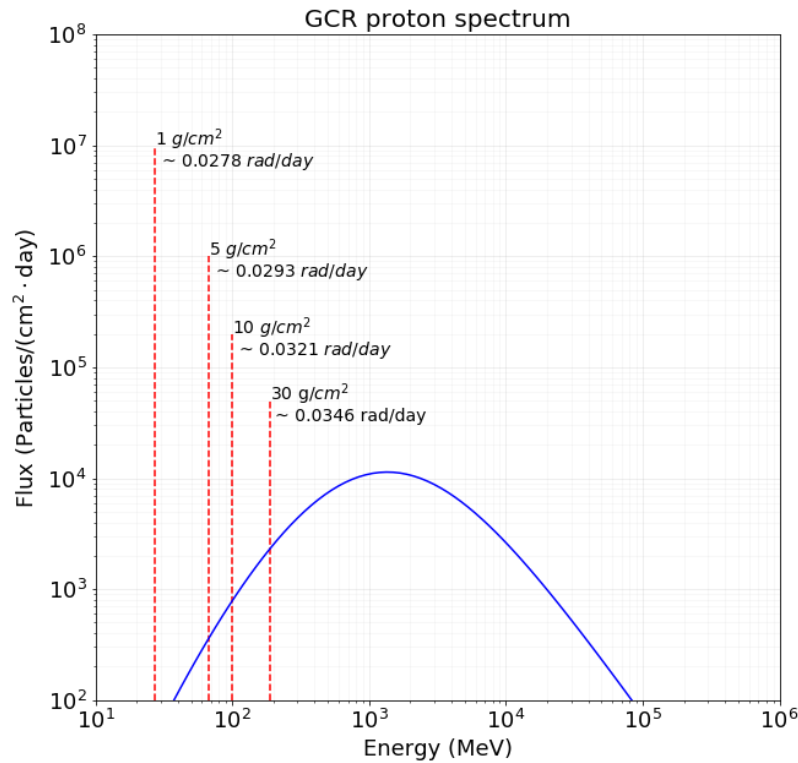


**Figure A3: GCR proton spectrum assumed in the presented analysis. The red-hashed line represents the proton energy corresponding to the range (in Al) shown at the top. The dose-rate represents an estimate of the exposure (in Si) behind an aluminum shield of the listed thickness.**